

# Far-Infrared Graphene Plasmonic Crystals for Plasmonic Band Engineering

Kitty Y. M. Yeung,<sup>†</sup> Jingyee Chee,<sup>†</sup> Hosang Yoon,<sup>†</sup> Yi Song,<sup>‡</sup> Jing Kong,<sup>‡</sup> and Donhee Ham<sup>\*,†</sup>

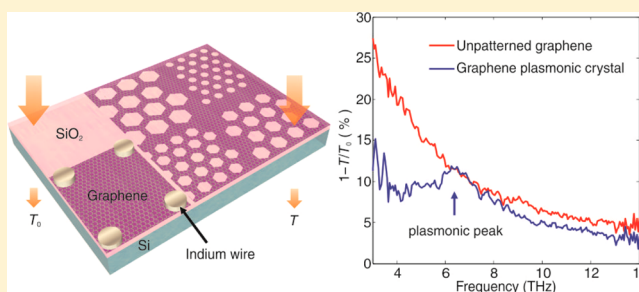
<sup>†</sup>School of Engineering and Applied Sciences, Harvard University, Cambridge, Massachusetts 02138, United States

<sup>‡</sup>Department of Electrical Engineering and Computer Science, Massachusetts Institute of Technology, Cambridge, Massachusetts 02139, United States

## Supporting Information

**ABSTRACT:** We introduce far-infrared graphene plasmonic crystals. Periodic structural perturbation—in a proof-of-concept form of hexagonal lattice of apertures—of a continuous graphene medium alters delocalized plasmonic dynamics, creating plasmonic bands in a manner akin to photonic crystals. Fourier transform infrared spectroscopy demonstrates band formation, where far-infrared irradiation excites a unique set of plasmonic bands selected by phase matching and symmetry-based selection rules. This band engineering may lead to a new class of graphene plasmonic devices.

**KEYWORDS:** Graphene, plasmonics, band engineering, plasmonic crystals, photonic crystals, far-infrared, terahertz



Graphene plasmons feature technologically significant attributes such as subwavelength confinement and tunability.<sup>1,32</sup> Thus, the first observation of plasmonic resonance in graphene with far-infrared excitation<sup>2</sup> has spurred a surge of efforts to engineer graphene plasmons.<sup>3–8</sup> These efforts have largely focused on *localized* plasmonic resonance within a specifically shaped graphene “island” such as a ribbon,<sup>2–5</sup> ring,<sup>6,7</sup> or disk,<sup>6–8</sup> defining its frequency with the boundary condition set by the island geometry. While these foundational works arrange the graphene islands in periodic arrays, the array has served only as a structural repetition to enhance gross plasmonic absorption by summing up each independent localized effect.

As an exception, it has been shown with an array of disk islands<sup>6</sup> that electrostatic coupling between proximate islands offers an additional mechanism to control the localized plasmonic resonance frequency in each island. This result<sup>6</sup> suggests one way to engineer the global dynamics across an array of graphene islands using its periodicity, despite the plasmon localization. In fact, engineering wave dynamics by medium periodicity is one hallmark paradigm to create wave-based devices. In contrast to ref 6, this principle can be applied to *delocalized* plasmons in a *continuous* graphene medium with a periodic structural perturbation, so as to pursue plasmonic band engineering in a manner akin to photonic crystals.<sup>9</sup>

Here we create such graphene plasmonic crystals by introducing a hexagonal array of apertures in a graphene sheet. Delocalized plasmons interact with the medium periodicity, forming a plasmonic band structure. This is demonstrated by resonantly coupling a far-infrared light into particular plasmonic modes belonging to a unique set of

plasmonic bands, where the light selects these specific modes because the spatial symmetry of the radiation field matches that of the plasmons within those modes. Our work is a step toward graphene plasmon band engineering, paving avenues for novel graphene plasmonic devices. Incidentally, a recent e-print<sup>10</sup> reports mid-infrared plasmon excitation in a similar aperture array; while sharing similar physics, it focuses on coupling graphene plasmons with mid-infrared substrate phonons—in contrast, we purposefully avoid such coupling by working in the far-infrared regime to focus on the medium-periodicity-based plasmon band engineering and symmetry-based plasmon band selection rule.

One can imagine a variety of ways to introduce structural periodicity in a continuous graphene medium. The hexagonal lattice of apertures in our work is one proof-of-concept realization of the medium periodicity. We fabricate four graphene plasmonic crystals, which we call GPC1 to GPC4 (Figure 1a), by etching out hexagonal lattices of circular (GPC1) or hexagonal shape apertures (GPC2 to GPC4) via photolithography in four separate regions of the same  $1.5 \times 1.5$  cm<sup>2</sup> graphene sheet. This graphene sheet, which is grown by chemical vapor deposition (CVD) and is transferred onto a 289 nm SiO<sub>2</sub>/381 μm Si substrate, exhibits the typical Raman spectrum (Figure 1b) of monolayer graphene.<sup>11,12</sup> The hexagonal lattice geometry of each plasmonic crystal occupying an area of  $2 \times 2$  mm<sup>2</sup> is characterized by the lattice constant  $a$ , the aperture shape that is circular or hexagonal, and the

**Received:** January 14, 2014

**Revised:** March 13, 2014

**Published:** March 28, 2014

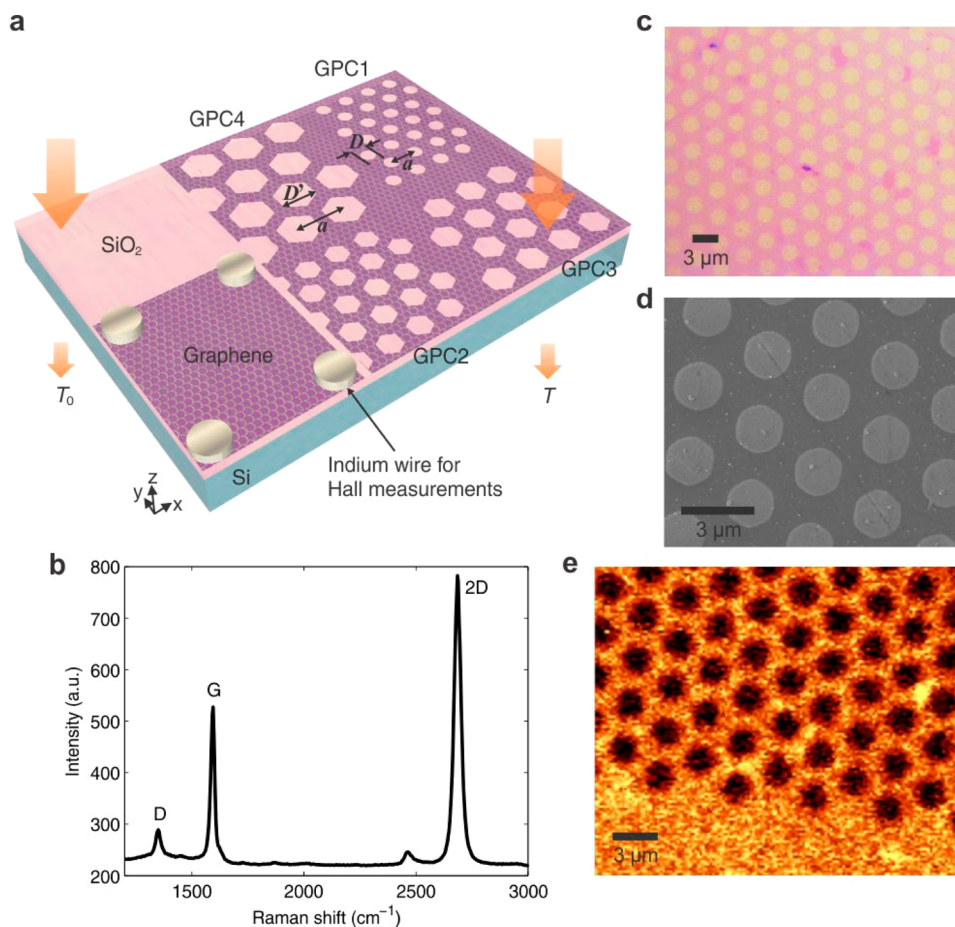


**Figure 1.** (a) Illustration (not drawn to scale) of our graphene sample on SiO<sub>2</sub>/Si substrate, containing four graphene plasmonic crystals: GPC1 ( $a \sim 3 \mu\text{m}$ ,  $D \sim 2 \mu\text{m}$ ), GPC2 ( $a \sim 4 \mu\text{m}$ ,  $D' \sim 3 \mu\text{m}$ ), GPC3 ( $a \sim 5 \mu\text{m}$ ,  $D' \sim 4 \mu\text{m}$ ), GPC4 ( $a \sim 6 \mu\text{m}$ ,  $D' \sim 5 \mu\text{m}$ ), an unpatterned graphene region, and bare SiO<sub>2</sub>/Si region uncovered by graphene.  $T [T_0]$  is the light intensity transmitted through a crystal [bare SiO<sub>2</sub>/Si] in FTIR. (b) Typical Raman spectrum of the graphene sample in the unetched area. (c) Optical image, (d) SEM image, and (e) integrated graphene Raman 2D peak intensity map from 2630 to 2730 cm<sup>-1</sup> of GPC1, with dark areas indicating apertures.

aperture size (diameter  $D$  in case of circular apertures, edge-to-opposite-edge distance  $D'$  in the case of hexagonal apertures). The geometric parameters are in the micrometer range; for instance,  $a$  ranges from 3 to 6  $\mu\text{m}$ . An optical micrograph and a scanning electron microscopy (SEM) image of GPC1 ( $a \sim 3 \mu\text{m}$ ;  $D \sim 2 \mu\text{m}$ ) are in Figures 1c,d. The map of the integrated Raman 2D peak intensity<sup>12,13</sup> from 2630 to 2730 cm<sup>-1</sup> (Figure 1e) also confirms the hexagonal lattice in the graphene.

We also leave a certain region unpatterned (area:  $\sim 1.0 \times 0.5 \text{ cm}^2$ ) in the same graphene sheet, as its interaction with far-infrared light provides a comparison to the interaction of plasmonic crystals with far-infrared light. On this unpatterned graphene, we also perform a Hall transport measurement via the four-probe Van der Pauw method from which we determine the charge carrier type (holes), its concentration  $n$  ( $\sim 1.05 \times 10^{13} \text{ cm}^{-2}$ ), and mobility  $\mu$  ( $\sim 1360 \text{ cm}^2/(\text{V s})$ ). These values correspond to a Fermi level  $E_F = -\hbar v_F(n\pi)^{1/2} \sim -0.38 \text{ eV}$  and carrier scattering time  $\tau = \hbar^2 \pi n \mu / (e E_F) \sim 5 \times 10^{-14} \text{ s}$  ( $\hbar$ : Planck constant;  $v_F$ : Fermi velocity;  $e$ : elementary charge).<sup>15</sup>  $E_F$  and  $\tau$  are important characteristics that influence the detailed behavior of graphene plasmons. While  $E_F$  and  $\tau$  spatially vary in large-area graphene<sup>14</sup> and also may assume degraded values in the patterned graphene plasmonic crystals due to the edge disorder introduced at the boundaries of the apertures,<sup>33</sup> their grossly measured values in the unpatterned region give a rough

feel for their values in the crystal regions and signify certain characteristics of the graphene sample. For instance, our graphene sample is strongly doped (with holes), and plasmonic quality  $Q = \omega\tau$  ( $\omega$ : angular frequency) is  $\sim 1.9$  at 6 THz.

The length scales of the hexagonal lattice parameters  $a$ ,  $D$ , and  $D'$  are comparable to the graphene plasmonic wavelengths in the far-infrared region, where graphene plasmons emerge conspicuously.<sup>1</sup> Hence, plasmons are scattered by the lattice, and their dispersion relation is transformed from the continuous dispersion curve of unpatterned graphene<sup>16</sup> into a plasmonic band structure, as seen theoretically.<sup>16,17</sup> We first show the plasmonic band structure of our hexagonal lattice by simulation, by solving Maxwell's equations via the finite element method with appropriate boundary conditions using COMSOL Multiphysics. Here graphene is modeled as a 0.5 nm thick conducting boundary layer with a conductivity corresponding to the intraband transitions at room temperature:<sup>18</sup>

$$\sigma(\omega, E_F, \tau) = -j \frac{e^2 E_F}{\pi \hbar^2} \frac{1}{\omega - j/\tau}$$

Bloch boundary conditions were used to represent the periodic structure. The material properties of the substrate are obtained from tabulated data.<sup>19</sup> The simulated band structure for GPC1 is displayed in Figure 2a (horizontal axis: plasmonic wave-number,  $k_p$ ; vertical axis: frequency,  $f$ ), where the 11 lowest-

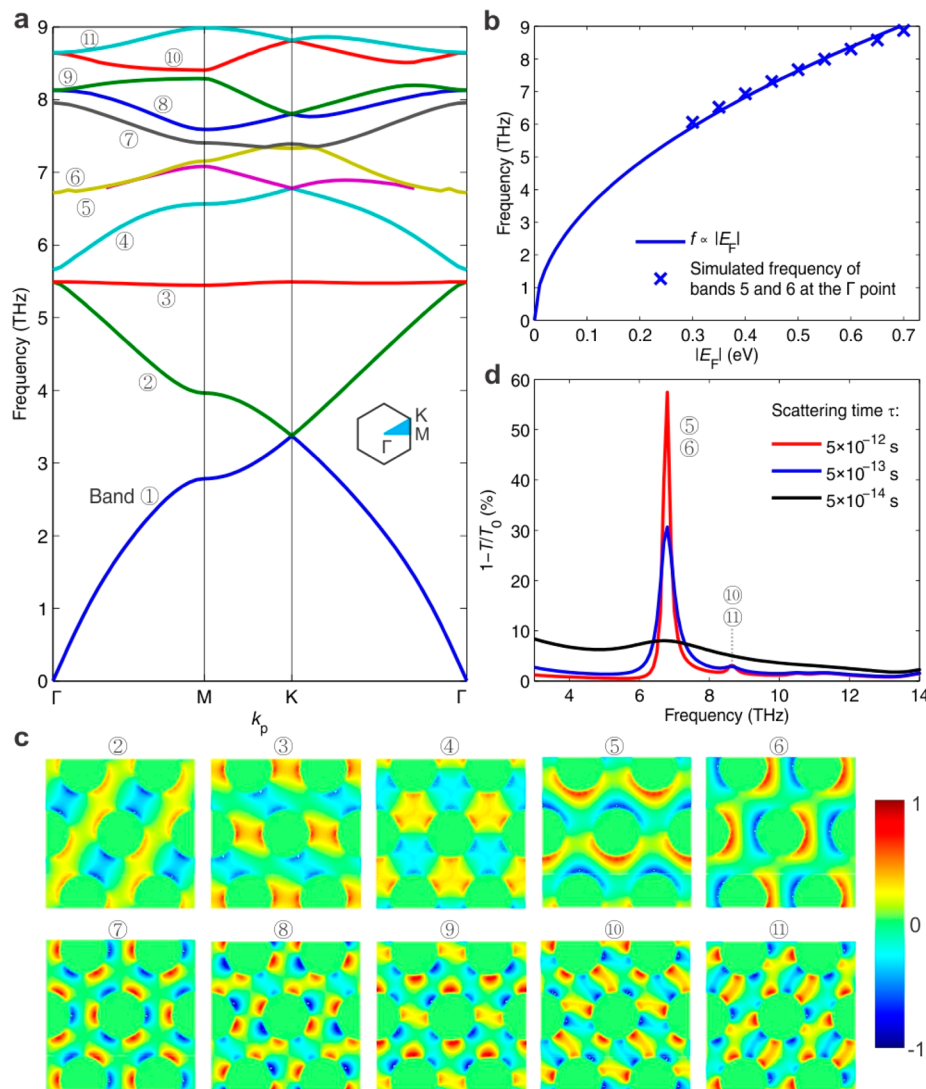


**Figure 2.** (a) Simulated band structure of GPC1 ( $E_F = -0.38$  eV) along high symmetry points of a hexagonal reciprocal lattice (inset). (b) Simulated frequencies of degenerate  $\Gamma$ -point plasmonic modes on bands 5 and 6 with varying  $E_F$  and a least-squares fit to  $f \propto \sqrt{|E_F|}$ . (c) Simulated  $E_{p,z}$  just above graphene for each  $\Gamma$ -point mode. Color bar shows normalized field strength. (d) Simulated extinction spectra of GPC1 for various  $\tau$  values. For (c) and (d)  $E_F = -0.38$  eV is used as in (a).

lying bands are shown along the high-symmetry points in reciprocal space. For this particular simulation, we use  $E_F = -0.38$  eV, obtained in the unpatterned region, as the exact value of  $E_F$  of the crystal is unknown. Simulations with differing  $E_F$  values reveal that the band diagram scales vertically in proportion to  $\sim\sqrt{|E_F|}$ , which is a key signature of graphene plasmons.<sup>1,2</sup> For example, Figure 2b shows this  $E_F$  dependency of the degenerate mode frequency of plasmonic bands 5 and 6 at the  $\Gamma$ -point.

To demonstrate the plasmonic band formation in the graphene plasmonic crystal, we perform Fourier transform infrared spectroscopy (FTIR) at room temperature by normally irradiating an unpolarized far-infrared plane wave along the  $z$ -axis onto the device lying in the  $x$ - $y$  plane. The wave vector  $k$  of the normally incident light has no component in the plane of the graphene, yet the corresponding  $k_x = k_y = 0$  line can still excite plasmonic modes at the  $\Gamma$  point ( $k_p = 0$ ) on the bands; such phase-matching and resultant plasmonic excitation would not be possible in unpatterned graphene, which exhibits a

continuous plasmonic dispersion relation with no plasmonic band formation.

Among all available  $\Gamma$ -point plasmonic modes, only two pairs of degenerate  $\Gamma$ -point modes belonging to bands 5 and 6 and bands 10 and 11 can be excited because the spatial symmetry of these specific plasmonic modes matches the spatial symmetry of the fields of the normally incident plane waves.<sup>20,21,29</sup> All other  $\Gamma$ -point modes behave differently than the radiation fields under symmetry operations (such as reflections with respect to planes parallel to the  $z$ -axis or rotations about the  $z$ -axis) and thus cannot be excited despite their phase matching to the normally incident wave. To help appreciate this, we illustrate the symmetries of all  $\Gamma$ -point plasmonic modes of the 11 lowest-lying bands by displaying the simulated spatial profiles of their electric field in the  $z$ -direction,  $E_{p,z}$ , just above the graphene (Figure 2c). The  $\Gamma$ -point plasmonic mode belonging to band 7, for example, has a  $120^\circ$  rotational symmetry about the  $z$ -axis, a symmetry that radiation fields do not possess, and thus it cannot be excited.

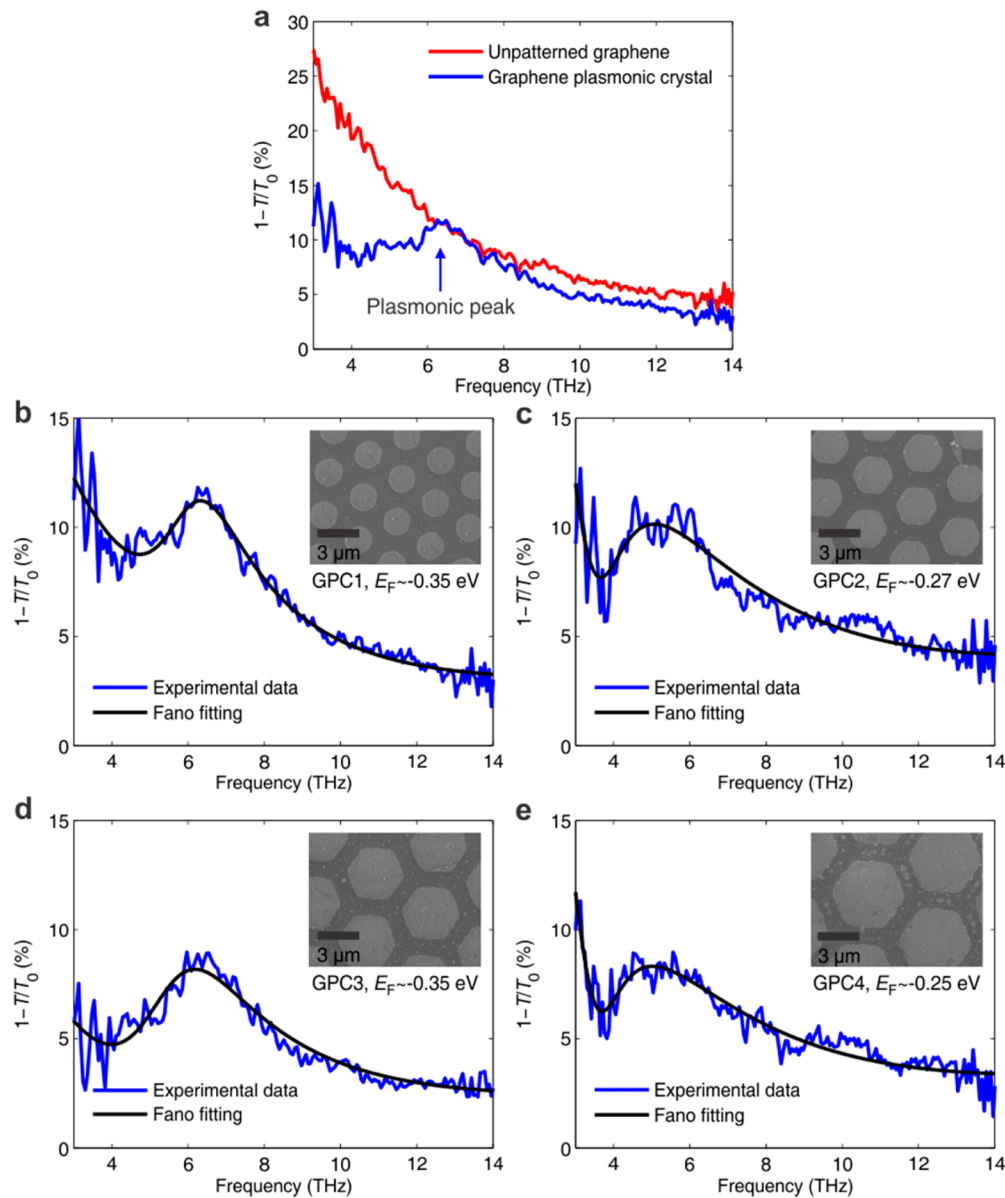


**Figure 3.** (a) Extinction spectra of unpatterned graphene (red) and GPC1 (blue), measured by FTIR spectroscopy. (b–e) Extinction spectra (blue) of GPC1–GPC4, least-squares fits (black) to an expression based on a Fano resonance. The grossly estimated value of  $E_F$  by simulation peak fitting (main text) is indicated for each crystal. The insets are SEM images of the crystals.

This symmetry-based selection rule can be formally proved. The hexagonal lattice possesses the  $C_{6v}$  point group symmetry, and thus, each  $\Gamma$ -point mode hosted by the lattice exhibits definite symmetry transformation properties under any symmetry operation belonging to the  $C_{6v}$  group. However, one can show that the symmetry transformation properties of only the degenerate  $\Gamma$ -point modes on bands 5 and 6 and those on bands 10 and 11 match the symmetry transformation properties of normally incident plane waves, being described by the same irreducible representation of the  $C_{6v}$  group (see Supporting Information).<sup>21,34</sup>

Simulation supports this selective plasmonic excitation. We solve Maxwell's equations with a plane-wave excitation to obtain the extinction,  $1 - T/T_0$  ( $T$  and  $T_0$  are the light intensity transmitted through the on-substrate graphene device of concern and through the substrate only, respectively; Figure 1a), which indicates the degree of absorption or reflection by the device. Figure 2d displays simulated extinction spectra of

GPC1 with  $E_F = -0.38$  eV for differing values of  $\tau$ . Simulation with either  $x$ - or  $y$ -polarized excitation light gives the same result. For  $\tau = 5 \times 10^{-12}$  s—this relatively long scattering time is feasible with high-mobility exfoliated graphene<sup>22,23</sup>—the extinction spectrum exhibits two peaks, confirming the selective excitation; the tall 6.8 THz peak (small 8.6 THz peak) is due to the excitation of the degenerate  $\Gamma$ -point plasmonic modes exactly at the same frequency on bands 5 and 6 (bands 10 and 11) in Figure 2a. These peaks, which can also be designed to occur in the mid-infrared,<sup>10</sup> are due to Fano resonances between the plasmon modes and direct transmission through the graphene, similar to the Fano resonance in photonic crystal slabs.<sup>9</sup> With decreasing  $\tau$  that lowers the plasmon quality factor,<sup>24,25</sup> each peak grows shorter and broader in simulation. For  $\tau = 5 \times 10^{-14}$  s that is commensurate with the mobility of our CVD-grown graphene, the peak due to the degenerate  $\Gamma$  point on bands 5 and 6 remains observable at a slightly lowered frequency (6.7 THz), while the peak due to the degenerate  $\Gamma$

point on bands 10 and 11 is unresolvable. Simulated extinction spectra with different geometric parameters show the same behavior (Supporting Information); in the low scattering regime, the extinction shows multiple peaks corresponding to a subset of  $\Gamma$ -point plasmonic modes allowed by the symmetry selection rule; in the high scattering regime (as in CVD graphene), a single broad peak appears, typically around the originally dominant peak.

Our work employs lower-mobility CVD graphene with  $\tau \sim 5 \times 10^{-14}$  s, for its large area is amenable to maximal coupling with the far-infrared beam from an Ever-Glo IR source (beam diameter:  $\sim 8.75$  mm). To ensure the measurement of only one particular plasmonic crystal under test, a mask with a pinhole (diameter  $\sim 2$  mm) is aligned right behind the particular crystal to permit only its signal transmitted. Thus, we expect from the simulation that the extinction spectrum will exhibit a single broad peak. In fact, the measured spectrum (Figure 3a, blue) of a GPC1 in the frequency range of 3–14 THz (above the lower cutoff frequency of a Thermo Fisher FTIR6700 system used and below the absorption bands of  $\text{SiO}_2$ ) exhibits a single broad peak near 6 THz with an overall decreasing background, in agreement with the shape of the extinction spectrum simulated with  $\tau = 5 \times 10^{-14}$  s. (The measurement is done in a  $\text{N}_2$  atmosphere with a polyethylene windowed far-IR deuterated triglycine sulfate detector; the transmission spectrum of  $\text{N}_2$  is separately measured, and this background spectrum is subtracted from every device spectrum.) This peak is due to the excitation of the degenerate  $\Gamma$ -point plasmonic modes on bands 5 and 6. The emergence of the peak demonstrates the band structure formation by the periodic structuring. This is because in unpatterned graphene the plasmonic dispersion curve does not form bands and thus cannot meet with the  $k_x = k_y = 0$  line representing the normally incident light. This lack of coupling between the light and plasmons in unpatterned graphene is clearly seen in the measured extinction of the unpatterned graphene region (Figure 3a, red). The monotonic spectrum is due to the background interaction between the light and graphene free carriers<sup>2</sup> (Supporting Information); no peak is observed due to the lack of light–plasmon coupling.

We can obtain the extinction peak frequencies by fitting the experimental spectra to a single-peak Fano resonance line shape<sup>26</sup>

$$1 - \frac{T}{T_0} = AT_B(\omega) \frac{\left( q_f + \frac{2(\omega - \omega_0)}{\Gamma_p} \right)^2 + b}{1 + \left( \frac{2(\omega - \omega_0)}{\Gamma_p} \right)^2}$$

where fitting parameters are  $A$  (amplitude),  $q_f$  (Fano parameter),  $\Gamma_p$  (plasmon damping rate),  $\omega_0$  (natural frequency), and  $b$  (screening parameter). Here  $T_B$  is the background extinction spectrum obtained experimentally from transmission through unpatterned graphene (Figure 3a, red). This single Fano resonance fit well approximates the single broad extinction peak in each graphene plasmonic crystal in the heavy carrier scattering regime (Supporting Information), and the  $R^2$  statistics of the fits are in the range of 0.88–0.95. The peak frequency obtained this way, 6.3 THz, is close to the simulated peak frequency at 6.7 THz. The  $\sim 5\%$  difference from the simulation is largely due to spatial variations in  $E_F$ ; that is,  $E_F = -0.38$  eV used in the simulation is from the unpatterned graphene region, while the crystal region under test in general assumes a different  $E_F$  value.

The observation of a single plasmon peak is robust across the remaining three plasmonic crystals with differing hexagonal lattice geometries (Figure 3b–e), further affirming the formation of the plasmonic band structure by the periodic patterning. As expected, the peak frequency varies from device to device because the band structure is altered with the lattice geometry. In our setup, the dependency of the peak frequency solely on geometric parameters (Supporting Information) cannot be closely examined, due in part to the photolithographic inaccuracy in controlling the geometric parameters to submicrometer precision and more fundamentally because  $E_F$  varies from device to device and from region to region even within a single device (spatial variations of  $E_F$  on CVD graphene can be on the order of 0.1 eV<sup>14,27</sup>). In fact, we estimate the gross effective  $E_F$  of each plasmonic crystal by matching the peak frequency between the measured and simulated spectrum, where the simulation uses  $E_F$  as a fitting variable and size and shape of the apertures estimated from the SEM as fixed parameters ( $\tau$  is kept at  $\sim 5 \times 10^{-14}$  s in this simulation because extinction peak frequencies are not sensitive to  $\tau$ , as far as  $\tau$  varies within the range expected for CVD graphene); the device-to-device variation of  $E_F$  so estimated is up to  $\sim 0.1$  eV (Figure 3b–e).

We further confirm the plasmonic origin of the observed peak by upshifting the overall  $|E_F|$  distribution across the entire sample containing the four crystals via global chemical doping of holes and by verifying if the peak frequency of each crystal increases. This method is beneficial in the face of the device-to-device variation of  $E_F$  since it does not require the exact knowledge of the spatial distribution of  $E_F$ . After chemically hole-doping the sample by exposure to 70%  $\text{HNO}_3$  vapor for 1 min, which increases the measured  $E_F$  from  $-0.38$  to  $-0.55$  eV in the unpatterned region, the measured peak frequency in every crystal shifts upward consistently (Figure 4), reaffirming

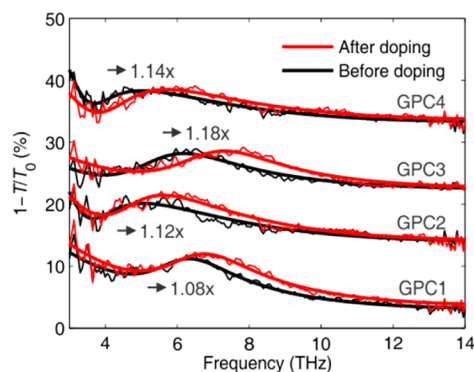


**Figure 4.** Extinction spectra (thin lines) of the four graphene plasmonic crystals before (black) and after (red) hole doping. The factor by which the peak frequency increases is shown for each crystal. Bold lines are least-squares fits to an expression based on the Fano resonance. A vertical cumulative offset of 10% is added between the spectra from different crystals for clarity.

the plasmonic origin of the spectral peaks. Incidentally, the frequency upshift factor indicated in Figure 4 is not constant among the devices because the predoping  $E_F$  spatial profile is nonuniform, doping itself may not be perfectly uniform, and the *ex situ* doping procedure may cause a slightly different crystal position to be probed by the FTIR before and after doping.

The demonstrated interaction of delocalized graphene plasmons with medium periodicity to form plasmonic bands may open up exciting new avenues for a wealth of subwavelength graphene plasmonic devices based on plasmonic band engineering, such as band gap filters, modulators, switches, and metamaterials.<sup>25,28,35</sup> While the symmetry-based selective excitation played a key role in demonstrating the formation of the plasmonic band structure in the present work, other coupling schemes<sup>30,31</sup> may enable the presently latent plasmon bands to be excited and probed. Higher quality factor devices are also expected in the near future, as the mobility of large-area CVD graphene continues to improve and the area of high-mobility exfoliated graphene continues to increase.<sup>22,23</sup>

## ■ ASSOCIATED CONTENT

### 📄 Supporting Information

Group-theoretical discussion on symmetry-based selection rules for excitable plasmonic bands and modes; simulated extinction spectra of the graphene plasmonic crystals; extinction spectra of unpatterned graphene calculated via the scattering matrix method; simulations showing effects of shape and size of the aperture on the extinction peak. This material is available free of charge via the Internet at <http://pubs.acs.org>.

## ■ AUTHOR INFORMATION

### Corresponding Author

\*E-mail: donhee@seas.harvard.edu (D.H.).

### Author Contributions

K.Y.M.Y. and J.C. contributed equally.

### Notes

The authors declare no competing financial interest.

## ■ ACKNOWLEDGMENTS

Donhee Ham acknowledges the support of this research by the Air Force Office of Scientific Research under contract FA9550-13-1-0211, the Office of Naval Research under contract N00014-13-1-0806, and the National Science Foundation under contract DMR-1231319. Jingyee Chee acknowledges financial support from National Science Scholarship, Singapore. Yi Song and Jing Kong acknowledge the support of Graphene Approaches to Terahertz Electronics (GATE) MURI through the Office of Naval Research. The authors thank Nuno Peres and Yuliy Bludov of University of Minho and Ian W. Frank of Harvard University for valuable discussions.

## ■ REFERENCES

- (1) Grigorenko, A. N.; Polini, M.; Novoselov, K. S. *Nat. Photonics* **2012**, *6*, 749–758.
- (2) Ju, L.; Geng, B.; Horng, J.; Girit, C.; Martin, M.; Hao, Z.; Bechtel, H. A.; Liang, X.; Zettl, A.; Shen, Y. R.; Wang, F. *Nat. Nanotechnol.* **2011**, *6*, 630–634.
- (3) Yan, H.; Low, T.; Zhu, W.; Wu, Y.; Freitag, M.; Li, X.; Guinea, F.; Avouris, P.; Xia, F. *Nat. Photonics* **2013**, *7*, 394–399.
- (4) Brar, V. W.; Jang, M. S.; Sherrott, M.; Lopez, J. J.; Atwater, H. A. *Nano Lett.* **2013**, *13*, 2541–2547.
- (5) Freitag, M.; Low, T.; Zhu, W.; Yan, H.; Xia, F.; Avouris, P. *Nat. Commun.* **2013**, *4*, 1951.
- (6) Yan, H.; Xia, F.; Li, Z.; Avouris, P. *New J. Phys.* **2012**, *14*, 125001.
- (7) Fang, Z.; Thongrattanasiri, S.; Schlather, A.; Liu, Z.; Ma, L.; Wang, Y.; Ajayan, P. M.; Nordlander, P.; Halas, N. J.; Garcia de Abajo, F. J. *ACS Nano* **2013**, *7*, 2388–2395.
- (8) Yan, H.; Li, X.; Chandra, B.; Tulevski, G.; Wu, Y.; Freitag, M.; Zhu, W.; Avouris, P.; Xia, F. *Nat. Nanotechnol.* **2012**, *7*, 330–334.
- (9) Fan, S.; Joannopoulos, J. D. *Phys. Rev. B* **2002**, *65*, 235112.

- (10) Zhu, X.; Wang, W.; Yan, W.; Larsen, M. B.; Bøggild, P.; Pedersen, T. G.; Xiao, S.; Zi, J.; Mortensen, N. A. arXiv:1312.2400, 2013.
- (11) Reina, A.; Jia, X.; Ho, J.; Nezich, D.; Son, H.; Bulovic, V.; Dresselhaus, M. S.; Kong, J. *Nano Lett.* **2009**, *9*, 30–35.
- (12) Li, X.; Cai, W.; An, J.; Kim, S.; Nah, J.; Yang, D.; Piner, R.; Velamakanni, A.; Jung, I.; Tutuc, E.; Banerjee, S. K.; Colombo, L.; Ruoff, R. S. *Science* **2009**, *324*, 1312–1314.
- (13) Malard, L. M.; Pimenta, M. A.; Dresselhaus, G.; Dresselhaus, M. S. *Phys. Rep.* **2009**, *473*, 51–87.
- (14) Yan, H.; Xia, F.; Zhu, W.; Freitag, M.; Dimitrakopoulos, C.; Bol, A. A.; Tulevski, G.; Avouris, P. *ACS Nano* **2011**, *5*, 9854–9860.
- (15) Das Sarma, S.; Adam, S.; Hwang, E. H.; Rossi, E. *Rev. Mod. Phys.* **2011**, *83*, 407–470.
- (16) Nikitin, A. Y.; Guinea, F.; Martin-Moreno, L. *Appl. Phys. Lett.* **2012**, *101*, 151119.
- (17) Bludov, Y. V.; Ferreira, A.; Peres, N. M. R.; Vasilevskiy, M. I. *Int. J. Mod. Phys. B* **2013**, *27*, 1341001.
- (18) Mock, A. *Opt. Mater. Exp.* **2012**, *2*, 771–781.
- (19) Palik, E. D. *Handbook of Optical Constants of Solids*; Academic Press: New York, 1985.
- (20) Kilic, O.; Dignonnet, M.; Kino, G.; Solgaard, O. *Opt. Exp.* **2008**, *16*, 13090–13103.
- (21) Sakoda, K. *Optical Properties of Photonic Crystals*, 2nd ed.; Springer: Berlin, 2005.
- (22) Du, X.; Skachko, I.; Barker, A.; Andrei, E. Y. *Nat. Nanotechnol.* **2008**, *3*, 491–495.
- (23) Dean, C. R.; Young, A. F.; Meric, I.; Lee, C.; Wang, L.; Sorgenfrei, S.; Watanabe, K.; Taniguchi, T.; Kim, P.; Shepard, K. L.; Hone, J. *Nat. Nanotechnol.* **2010**, *5*, 722–726.
- (24) Yeung, K. Y. M.; Yoon, H.; Address, W.; West, K.; Pfeiffer, L.; Ham, D. *Appl. Phys. Lett.* **2013**, *102*, 021104.
- (25) Address, W.; Yoon, H.; Yeung, K. Y. M.; Qin, L.; West, K.; Pfeiffer, L.; Ham, D. *Nano Lett.* **2012**, *12*, 2272–2277.
- (26) Gallinet, B.; Martin, O. J. F. *Phys. Rev. B* **2011**, *83*, 235427.
- (27) Chen, C.-F.; Park, C.-H.; Boudouris, B. W.; Horng, J.; Geng, B.; Girit, C.; Zettl, A.; Crommie, M. F.; Segalman, R. A.; Louie, S. G.; Wang, F. *Nature* **2011**, *471*, 617–620.
- (28) Yoon, H.; Yeung, K. Y. M.; Umansky, V.; Ham, D. *Nature* **2012**, *488*, 65–69.
- (29) Peres, N. M. R.; Bludov, Yu. V.; Ferreira, A.; Vasilevskiy, M. I. *J. Phys.: Condens. Matter* **2013**, *25*, 125303.
- (30) Zhu, X.; Yan, W.; Jepsen, P. U.; Hansen, O.; Mortensen, N. A.; Xiao, S. *Appl. Phys. Lett.* **2013**, *102*, 131101.
- (31) Gao, W.; Shi, G.; Jin, Z.; Shu, J.; Zhang, Q.; Vajtai, R.; Ajayan, P. M.; Kono, J.; Xu, Q. *Nano Lett.* **2013**, *13*, 3698–3702.
- (32) Yoon, H.; Forsythe, C.; Wang, L.; Tombros, N.; Watanabe, K.; Taniguchi, T.; Hone, J.; Kim, P.; Ham, D. arXiv:1401.4240, 2014.
- (33) Lee, E. J. H.; Balasubramanian, K.; Weitz, R. T.; Burghard, M.; Kern, K. *Nat. Nanotechnol.* **2008**, *3*, 486–490.
- (34) Painter, O.; Srinivasan, K. *Phys. Rev. B* **2003**, *68*, 035110.
- (35) Yoon, H.; Yeung, K. Y. M.; Kim, P.; Ham, D. *Philos. Trans. R. Soc., A* **2014**, *372*, 10.1098/rsta.2013.0104